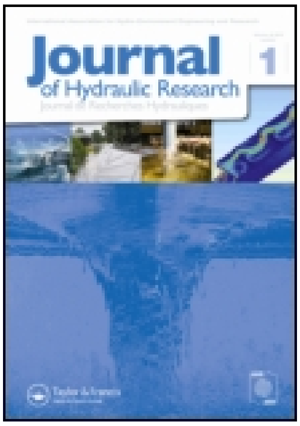

Journal of Hydraulic Research
Publication details, including instructions for authors and subscription information:
http://www.tandfonline.com/loi/tjhr20

Experimental study on sand bed excavation by impinging swirling jets

Joaquin Ortega-Casanova [a] , Nicolas Campos [b] & Ramon Fernandez-Feria [c]

[a] ETS de Ingenierı́ıa Industrial, Univ. de Mı́álaga, Dr Ortiz Ramos s/n, 29071, Mı́álaga, Spain

[b] ETS de Ingenierı́ıa Industrial, Univ. de Mı́álaga, Dr Ortiz Ramos s/n, 29071, Mı́álaga, Spain E-mail: nicalon@hotmail.com

[c] ETS de Ingenierı́ıa Industrial, Univ. de Mı́álaga, Dr Ortiz Ramos s/n, 29071, Mı́álaga, Spain E-mail: ramon.fernandez@uma.es

Available online: 26 Sep 2011

To cite this article: Joaquin Ortega-Casanova, Nicolas Campos & Ramon Fernandez-Feria (2011): Experimental study on sand bed excavation by impinging swirling jets, Journal of Hydraulic Research, 49:5, 601-610

To link to this article: http://dx.doi.org/10.1080/00221686.2011.593346

Journal of Hydraulic Research Vol. 49, No. 5 (2011), pp. 601–610
doi:10.1080/00221686.2011.593346

Research paper

Experimental study on sand bed excavation by impinging swirling jets

JOAQUIN ORTEGA-CASANOVA, Associate Professor, *ETS de Ingeniería Industrial, Univ. de Málaga, Dr Ortiz Ramos s/n, 29071 Málaga, Spain.*
Email: jortega@uma.es (author for correspondence)

NICOLAS CAMPOS, PhD Student, *ETS de Ingeniería Industrial, Univ. de Málaga, Dr Ortiz Ramos s/n, 29071 Málaga, Spain.*
Email: nicalon@hotmail.com

RAMON FERNANDEZ-FERIA, Professor, *ETS de Ingeniería Industrial, Univ. de Málaga, Dr Ortiz Ramos s/n, 29071 Málaga, Spain.*
Email: ramon.fernandez@uma.es

ABSTRACT
The excavation performance of swirling jets impinging normally against a sand bed from several distances is described. A specially-designed nozzle with adjustable swirl vanes was used to generate swirling jets of various swirl intensities. Two sand beds of different grain size distributions were considered. The main scour patterns on the sand bed produced by the swirling jets were measured by image processing of photographs of the bed illuminated by a laser sheet. The velocity profiles of the swirling jets at the nozzle exit were measured using Laser Doppler Anemometry for various test conditions. The scour patterns were then analysed in relation to the details of the velocity profile of the swirling jets, their Reynolds numbers and the distances from the nozzle to the bed. The optimum jet features resulting from the different swirl nozzles and the best impinging distances for sea bed excavation are identified and discussed.

Keywords: Erodible bed, scour, sediment transport, swirling jet, velocity profile

1 Introduction

The interaction of a jet impinging on a sediment bed has been investigated by researches in sea bed excavation, dredging and other underwater operations in coastal and marine engineering. Experimentation of the erosional action of water jets impinging on submerged sediment beds were conducted by Rouse (1940), both for jets kept at a fixed position relative to the sand bed (Rajaratnam and Berry 1977, Rajaratnam 1981, Aderibigbe and Rajaratnam 1996, Qi *et al*. 2000), or for travelling impinging jets (Peng and Capart 2008). Although the present investigation is not concerned with the erosion process itself, it is worth mentioning that theories have been proposed for the jet-induced erosion of non-cohesive sediment beds to explain the results (Hogg *et al*. 1997, Gioia and Bombardelli 2005, Bombardelli and Gioia 2006, Peng and Capart 2008). The present work is concerned with the physical characterization of the enhancing effects that the addition of a swirl velocity component to the impinging jet may have on the erosion and transport processes on a sand bed, to improve the jet excavation performance. Pulsating jets have been proved to have this enhancing effect and are considered more effective with regard to sediment erosion and transport than steady jets (Kobus *et al*. 1979). A related issue in coastal and marine engineering is propeller-induced scour (e.g. Hamill *et al.* 1999). The idea of using swirl to improve the excavation and dredging performances of submerged jets was originally proposed by Redding (2006) and developed in the "Swirl Jet Project" (2007). The results confirmed the eroding effect of the swirl superimposed to the standard impinging jet (Thomas *et al*. 2007, Felli *et al*. 2010). However, the results indicated that an increase of the excavation performance was not always due to the vortex breakdown phenomenon (e.g. Lucca-Negro and O'Doherty 2001) of the swirling jet, as originally proposed by Redding (2006), but due the axial flow intensification caused by the swirl (Ortega-Casanova *et al*. 2007, Thomas *et al*. 2007).

Revision received 30 May 2011/Open for discussion until 30 April 2012.

ISSN 0022-1686 print/ISSN 1814-2079 online
http://www.informaworld.com

To shed further light on this problem, the scour produced on sand beds was characterized experimentally by several types of swirling jets generated by special swirl nozzles. Their main scour features were quantitatively measured for various jet Reynolds numbers and distances between the nozzle and the undisturbed sand bed. The velocity fields at the swirl nozzle exits were measured using Laser Doppler Anemometry (LDA), so that the nozzle excavation performances may be explained in terms of the swirl jet details, the non-dimensional parameters governing the swirling jet and the distance to the sand bed. In all cases, a comparison with the scour produced by a non-swirling jet at identical conditions is included. To understand the excavation process, the quantitative measurements of the scour patterns are complemented with visualizations of the impinging swirling jet. All details of the experimental setup and the various experimental techniques used herein are described in the next section. Section 3 presents the experimental results and their discussion, while the main conclusions follow in Section 4.

2 Experimental setup and techniques

2.1 *Experimental rig*

Figure 1 shows a sketch of the test setup. A tank was used of square base area 1 m^2, 0.5 m deep mounted on an aluminium frame. Its surfaces are of Plexiglas to allow for flow visualizations using LDA and for photographs of the scour on the sand bed generated by the swirling jets. The sand was in a container at the tank bottom, while the upper tank portion was open to the atmosphere with a free surface of water through which the swirl generator nozzle is submerged. The nozzle was mounted on a precision height gauge (range of 0–300 mm, a dial reading of 0.01 mm and an accuracy of ± 0.03 mm) to adjust the vertical distance from the nozzle exit to the sand bed. Water was recirculated with a low pressure magnetically-coupled pump, leaving tank through two orifices at the upper part of the lateral surfaces, passing through a filter to retain suspended sand and decanted into a small auxiliary deposit. After passage through a stop valve, it was impelled by the recirculation pump to the swirl generator nozzle inside the tank. A stop valve was also incorporated downstream of the pump, in addition to an adjustable valve and a turbine flow metre to monitor the water discharge. The Pelton wheel turbine flow metre has a range of 0.5–15 l/min, with an estimated relative error of 1% in the digital display. The pump, and the valves, the filter and the flow metre were assembled with the auxiliary deposit on an adjoin table independent of the tank frame to avoid vibrations of the pump to the flow inside the tank.

For flow visualization and quantitative measurement of the scour pattern on the sand bed, a digital camera was mounted either on the top or at one side of the tank. The illumination was provided by a laser sheet from a green 532 nm laser of 40 mW. For flow visualization, it was set vertically, whereas for sand height data, it was inclined to the bed with the video-camera set perpendicularly to the laser sheet.

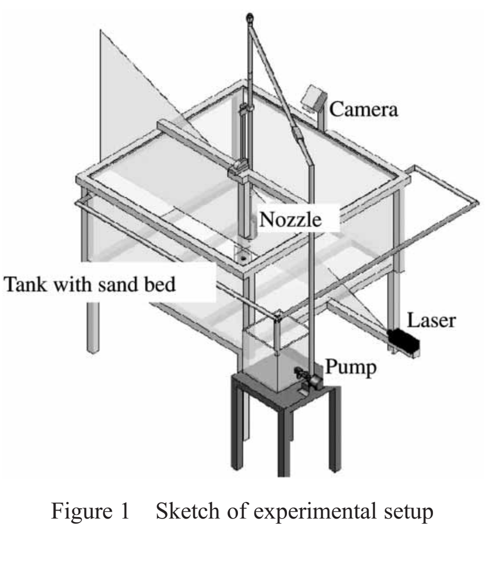

Figure 1 Sketch of experimental setup

2.2 *Swirl generator nozzles*

To generate the swirling jet, a nozzle was used whose tangential velocity is imparted to the flow by the use of swirl vanes with adjustable angles. These nozzles have been designed in-house by accounting for experience from a participation in the “Swirl Jet Project” (Ortega-Casanova *et al*. 2007). The vanes were mounted inside a cylindrical chamber (Fig. 2), at the bottom of which the nozzle of exit diameter $D = 5$ mm was located. The water flow enters the nozzle chamber through a pipe connected to its upper surface, slows down before attacking the swirl vanes at the chamber bottom part and exits as a swirling jet. This nozzle contains an inner body or hub to enhance the axial velocity at the axis induced by the swirl (see below). The

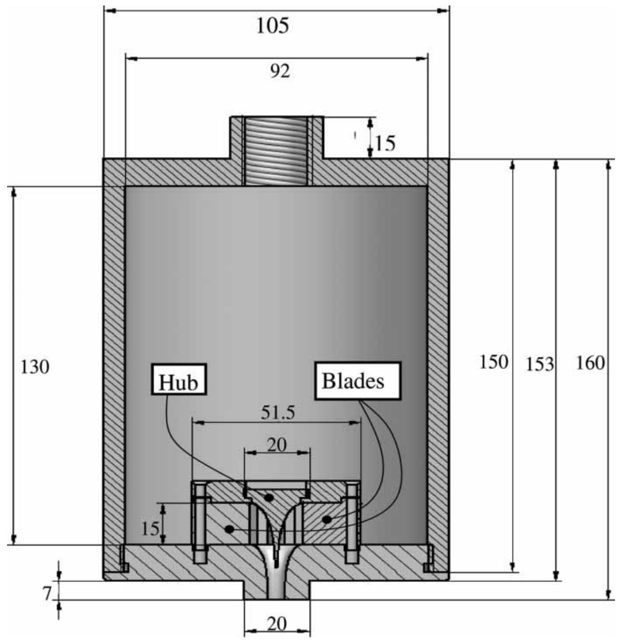

Figure 2 Nozzle configuration with stagnation chamber, set of swirl vanes and nozzle exit. Dimensions in mm

convenience of this inner body for generating swirling jets of interest to sea-bed excavation is discussed and detailed by Ortega-Casanova *et al*. (2007).

Numerical simulations of the flow inside nozzles are reported in the above reference, for nozzle configurations similar to that used herein indicate that the present design is such that an intense axial velocity overshoot of the vortex core is generated at the nozzle exit if a high swirl intensity is imparted to the flow by the vanes, while the axial velocity profiles at the nozzle exit are almost flat if the swirl is low or absent, as corroborated by the experimental data reported below.

Eight vane types were used to generate the swirling jet (Fig. 3), each mounted with five different angles, so that for a given nozzle Reynolds number, five swirling jets were generated for a given set, with five different swirl intensities. If the vanes are mounted radially, no swirl is imparted to the jet. The maximum swirl for each vane set results if they are mounted with the maximum angle between the incoming radial flow and the vanes (Fig. 3). The main difference between the different sets lies in the blade thickness. For identical discharge and vane angle, the nozzle mounted with thicker vanes generates a swirling jet of higher swirl intensity than thinner vanes.

Herein, only the results from three vane sets are reported, relating to the thickest blades (Fig. 3): a radial configuration, referred to as Case R, and two swirl configurations corresponding to the two most tangential vane positions, one with a vane angle of 15.6° (Case S1), and Case S2 as shown in Fig. 3. All remaining configurations resulted in less interest for seabed excavation. Case R was retained to compare its performance with the non-swirling jet case (Table 1).

2.3 *LDA measurements of velocity profiles at nozzle exit*

To characterize the velocity profiles generated by the swirl vanes for a given discharge, both the tangential and the axial velocity profiles were measured at the nozzle exit using LDA (Section 3.1). A one-dimensional (1D) LDA supplied by the company

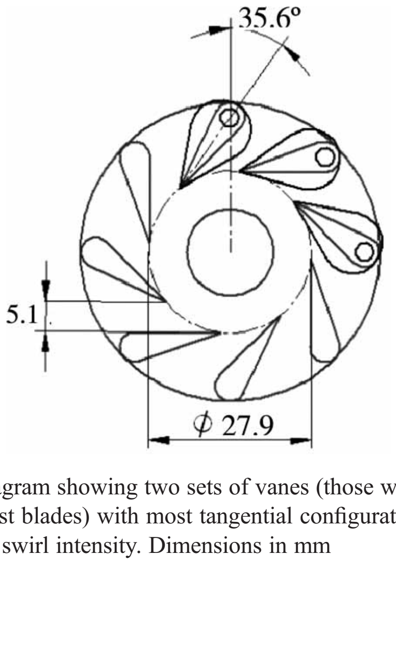

Figure 3 Diagram showing two sets of vanes (those with the thinnest and the thickest blades) with most tangential configuration, generating the maximum swirl intensity. Dimensions in mm

Table 1 Vane angles and dimensions of different configurations, with chord vane 17.57 mm long and maximum vane thickness of 5.2 mm

Case	Vane angle (°)
R	0
S1	15.6
S2	35.6

DANTEC was mounted on a 2D traversing system (Fig. 4). Both were controlled by the software BSA/FVA Flow (Dantec 2000). Both the axial and the tangential velocity components in a 2D grid were then measured at the nozzle exit.

The LDA data were taken in an experimental setup similar to that described above, but without both the sand bed and the precision height gauge: the nozzle was just immersed inside the water tank at a fixed distance from the plain bottom, but close enough to one of the lateral transparent walls to facilitate the LDA measurements. The water was seeded with silver-coated hollow glass particles of 10 μm diameter, supplied by DANTEC.

To compute the Reynolds number, the mean temperature T was used and the mean discharge Q, so that

$$\mathsf{R} = \frac{4\rho Q}{\mu \pi D}, \qquad (1)$$

where $D = 5$ mm is the nozzle exit diameter, and ρ and μ are the density and the viscosity of water, respectively, as functions of temperature T (White 2005)

$$\rho(\mathrm{kg/m^3}) = 1000 - 0.0178|T^{\circ}\mathrm{C} - 4^{\circ}\mathrm{C}|^{1.7} \pm 0.2\%, \qquad (2)$$

$$\ln\frac{\mu}{\mu_0} = -1.704 - 5.30x + 7.003x^2, \quad x = \frac{273\mathrm{K}}{T\mathrm{K}}, \quad \mu_0 = 1.788 \times 10^{-3}\mathrm{kg/(ms)}. \qquad (3)$$

Figure 4 Photograph of 1D LDA system mounted on 2D automatic traversing system to measure velocity profiles at nozzle exit. LDA characteristics: Laser He–Ne of 10 mW, wavelength 632.8 nm (red), beam separation 38.4 mm, focal length 160.6 mm, beam angle at crossing 13.634°, with 29 fringes in volume sampling. Traversing length 590 mm, both in x and y directions; 40 mm/s maximum motor speed in both directions

2.4 *Sand parameters*

Two different sands were used: SAND1, from the beach of Málaga city, of mean grain diameter $d_{50} = 0.36$ mm, grain density of 2.60 g/cm^3, bulk density of 1.69 g/cm^3 and measured mean fall velocity in water of 0.07796 m/s, sediment non-uniformity coefficient $\sigma = (d_{84}/d_{16})^{1/2} = 1.48$; SAND2, a commercial sand, with grain size of $d_{50} = 1.40$ mm, grain density of 2.53 g/cm^3, bulk density of 1.60 g/cm^3, measured mean fall velocity in water of 0.22472 m/s and $\sigma = 1.50$. These sands are considered representative for sea bed conditions. Note that their gradations are similar, although the mean grain sizes differ.

2.5 *Quantitative measurement of scour patterns on sand bed*

Once the different flow configurations were characterized, the scour patterns were generated. The sand was inserted at the tank bottom, at a distance H from the nozzle exit, illuminated by a vertical laser sheet passing through the nozzle axis and the jet. The contour of the scour thus illuminated by the laser sheet was photographed with the video-camera set perpendicularly to the laser sheet, similar to Andreotti *et al.* (2006) to characterize aeolian sand ripples in the laboratory.

To reduce the deformation due to refraction and misalignment between the camera and the laser sheet, a preliminary image transformation was attempted. A calibration target with a matrix of white concave "dots" was employed. The actual distance between the centres of the "dots" was 2.5 mm. This target was positioned inside the tank, with the water at rest before running the jet, on the sand bed and in the same cross-section plane of the laser sheet where the subsequent images were captured. The image of the target was transformed into a square with its actual size by means of a bilinear transformation of a number of points. Since this transformation contained 12 unknown coefficients, at least 6 points of the target were selected and transformed into the calibrated points. The resulting transformation was then applied to all images of the sand bed and the swirling jet.

The sequence of a test was as follows: a picture of the target inside the water tank at rest was first taken resulting in the calibration coefficients and the ground level of the sand bed; then the target was removed, the swirling jet with a selected discharge was run until the scour hole remained steady; the jet was turned off, a picture of the scour illuminated by the laser sheet was taken once the sand bed had stabilized, and finally, this image was transformed using the calibration coefficients. Figure 5 shows an example, with (a) as the distorted image of the scour pattern, as captured by the camera, and (b) as the transformed image, corresponding to its actual shape on the normal plane to the bed. To digitalize the scour contours, a threshold segmentation technique to the images was applied (Young *et al.* 1996). Figure 6 shows an example of a scour pattern thus processed, after transforming pixels to actual distances, and using the

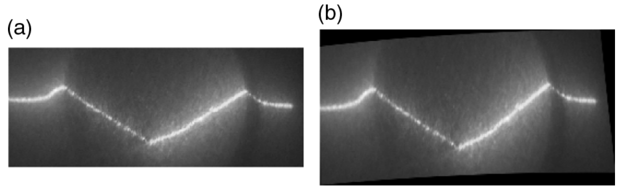

Figure 5 Images of scour illuminated with laser sheet (a) before, (b) after transformation resulting from calibration (Case S2, $H/D = 5$, $Q = 330$ l/h or $\mathsf{R} = 20{,}000$)

non-dimensional coordinates (r, z), scaled with the nozzle radius $D/2$, and the origin set at the intersection of the jet axis with the undisturbed sand bed.

To characterize the different scour contours, three non-dimensional parameters were used (Fig. 6), namely radius $r_{\max}$ where the scour reaches its maximum elevation, measured from the maximum depth, elevation $H_{\max}$ over the original sand bed level, and the maximum scour depth $|H_{\min}|$ measured from the original sand bed level. All were extracted from digitalized images, after using the threshold segmentation technique.

3 Results

3.1 *Velocity profiles at nozzle exit*

Figures 7–9 show the radial profiles of the non-dimensional axial W and tangential V velocity components at nozzle exits for various R. The radial coordinate r is scaled with the nozzle exit radius $D/2$ and the velocity components with the mean nozzle exit velocity $W_c = 4Q/\pi D^2$.

To fit these velocity profiles, a q-vortex, or Gaussian vortex, model was used as a simplification of Batchelor's trailing-line vortex (Batchelor 1964, Ash and Khorrami 1995), resulting in a good fit to velocity profiles for vane-guide-generated vortices (e.g. Leibovich 1978, Garg and Leibovich 1979). This model was corrected by "tanh"-like mixing layers that adjust the flow to the external fluid at rest, as is commonly used to approximate the mixing

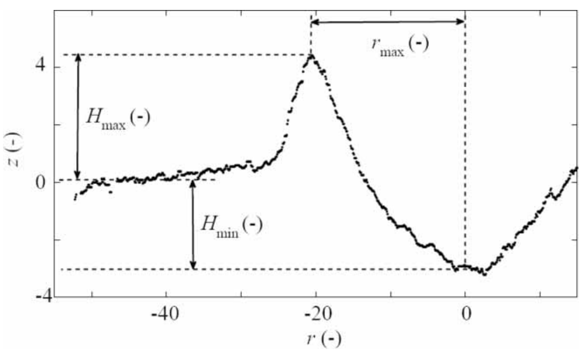

Figure 6 Digitized contour of scour in non-dimensional coordinates (r, z) and definitions of non-dimensional parameters $r_{\max}$, $H_{\max}$, $H_{\min}$ (Case S2, $H/D = 5$, $\mathsf{R} = 20{,}000$). Only a portion of right is shown. Data gaps due to occlusion of laser light by levee and scour imperfections

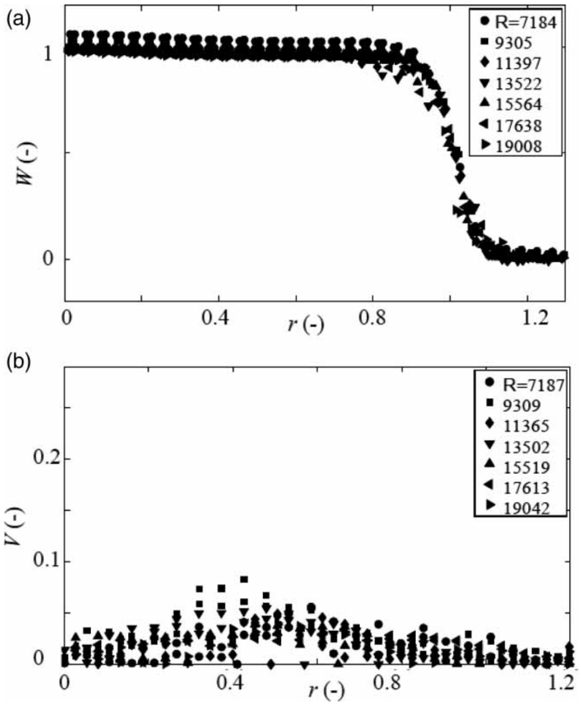

Figure 7 (a) Non-dimensional axial velocity W, (b) tangential velocity V components at exit of swirl nozzle for Case R and different R

layers of a jet discharging into a fluid at rest near the jet exit (e.g. Michalkxe 1984). The following expressions fit the velocity profiles

$$W = a\left(1 + b\mathrm{e}^{-(r/\delta_w)^2}\right)\frac{1}{2}\left(1 - \tanh\frac{r - r_w}{\delta_{w1}}\right), \tag{4}$$

$$V = \frac{q_v}{r}\left(1 - \mathrm{e}^{-(r/\delta_v)^2}\right)\frac{1}{2}\left(1 - \tanh\frac{r - r_v}{\delta_{v1}}\right), \tag{5}$$

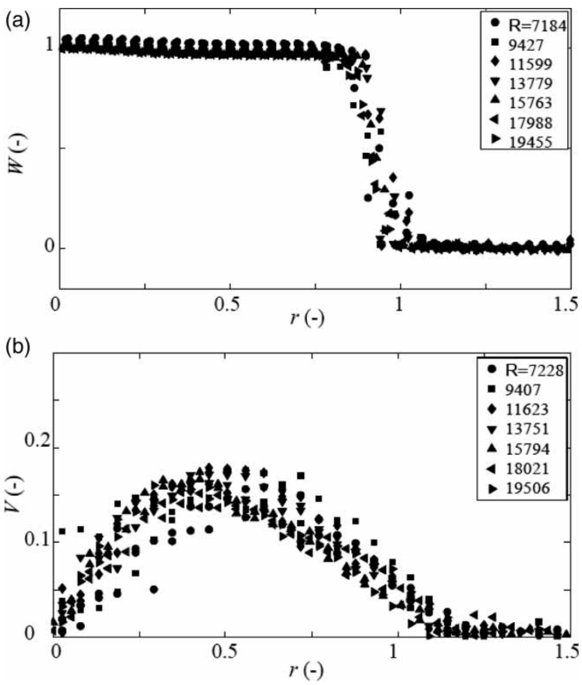

Figure 8 (a) Non-dimensional axial velocity W, (b) tangential velocity V components at exit of swirl nozzle for Case S1 and different R

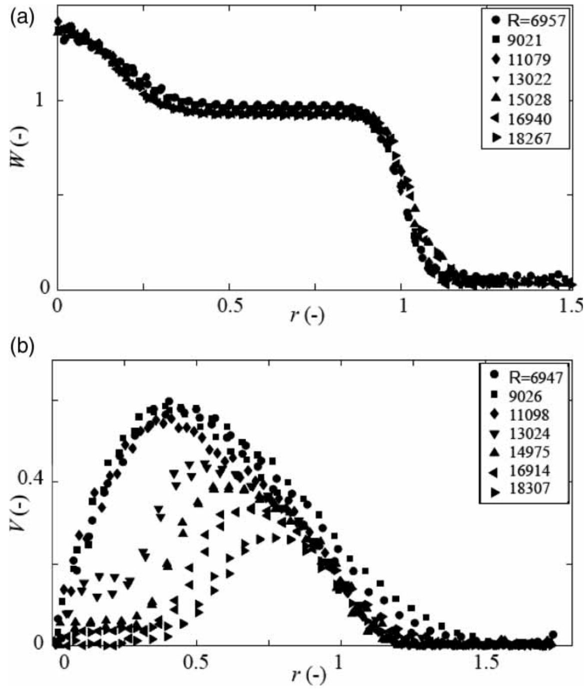

Figure 9 (a) Non-dimensional axial velocity W, (b) tangential velocity V components at exit of swirl nozzle for Case S2 and different R

where a, b, δ_w, r_w, δ_{w1}, q_v, δ_v, r_v and δ_{v1} are non-dimensional parameters (Figs 10 and 11). Note that q_v is a swirl number based on the axis vorticity and the nozzle exit radius $D/2$. Although the mixing layers are centred at $r = 1$ (i.e. $r_w = r_v = 1$), an optimum fit of these parameters was attempted. Also included in Fig. 11 is the data comparison of the tangential velocity component with the corresponding q-vortex, i.e. with Eq. (5) without the "tanh"-like term that multiplies the q-vortex, indicating that this term is necessary to fit the data well.

All measured axial velocity profiles fit Eq. (4) well, whereas $V(r)$ fits Eq. (5) well except for Case S2 if R $> 12{,}000$. As observed in Fig. 9, V near the axis drops abruptly in these cases, and the swirl velocity profile adopts a ring-like shape. These profiles may be fit by combining two Gaussian vortices, yet requiring a number of parameters, so that this was not made herein.

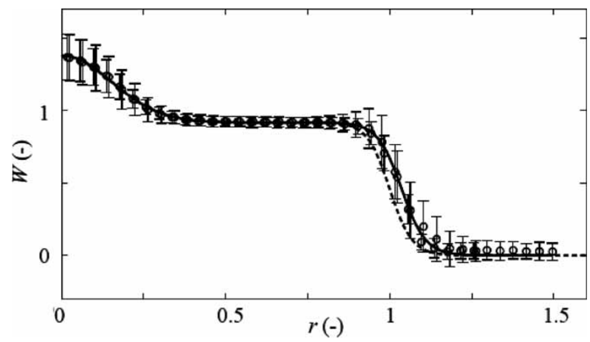

Figure 10 Comparison of (◦) mean axial velocity profiles for Case S2 and $Q = 160$ l/h (R $= 11{,}079$) with Eq. (4) using (– –) $a = 0.91950$, $b = 0.50179$, $\delta_w = 0.21497$, $\delta_{w1} = 0.07304$, $r_w = 1.03658$. (—) Fit to Eq. (4) with $r_w = 1$

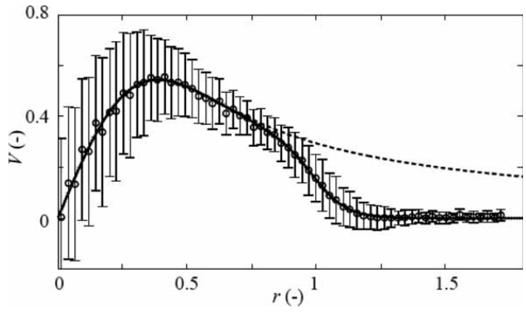

Figure 11 Comparison of measured $V(r)$ for ($\circ$) Case S2 and R = 11,098 (Q = 160 l/h) with Eq. (5) using ($--$) q_v = 0.2951, δ_v = 0.34844, δ_{v1} = 0.1338 and r_v = 1.004. (—) fit to Eq. (5) with r_v = 1, and with Eq. (5) without "tanh"-term and same values of q_v and δ_v (q-vortex)

The vortex core thickness δ_v is almost independent from R for a given vane configuration, slightly decreasing with R (Fig. 12a), except for the tangential velocity in Case S2 for high R. Note that $\delta_w < \delta_v$, yet their values are quite similar. The shear layer thicknesses (Fig. 12b) are practically independent from both R and the swirl configuration (again except for δ_{v1} for the tangential velocity in Case S2 for large R). Note that the shear layer for the axial velocity is slightly thinner than that for the tangential velocity.

To measure the swirl intensity, it is appropriate to define a swirl number q based on the vortex thickness $\delta = (D/2)\delta_v$, rather than on the nozzle radius $D/2$ used in q_v, i.e. (Ash and Khorrami 1995)

$$q = \frac{q_v}{\delta_v}. \tag{6}$$

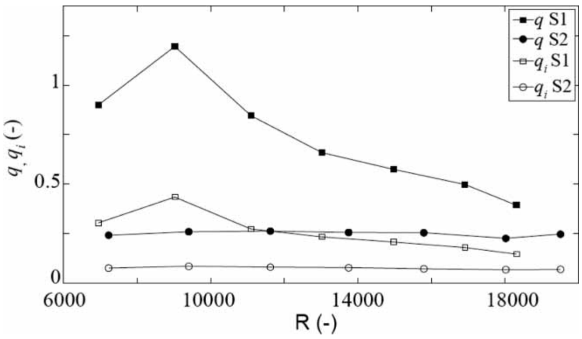

Figure 13 q and q_i versus R for various swirl vane configurations

Figure 13 shows q (R) for Cases S1 and S2. In Case S1, the swirl number is relatively small and practically independent of R. In Case S2, q first increases with R to a maximum and then decreases abruptly due to the tangential velocity drop at the axis above R = 12,000, so that Eq. (5) ceases to be valid, and q may no longer represent the jet swirl intensity. Note that this feature has nothing to do with vortex breakdown, because the corresponding axial velocity does not diminish. In fact, Fig. 11 shows that the axial velocity has a pronounced maximum at the axis for Case S2, which is almost identical for all R considered. This axial velocity overshoot is due to the swirl, i.e. the Gaussian in Eq. (4); note that $\delta_w \cong \delta_v$. It is almost imperceptible for Case S1 with a low swirl, but pronounced for Case S2 with a large swirl. This combination of intense axial velocity at the axis generated by the swirl, together with the annular radial profile of the circumferential velocity (low swirl near but high swirl off the axis) is most appropriate for excavation purposes.

To avoid problems with the swirl number q (or q_v) for high R with Case S2, when the maximum swirl is away from the jet axis, a third swirl number q_i based on integrals of the velocity

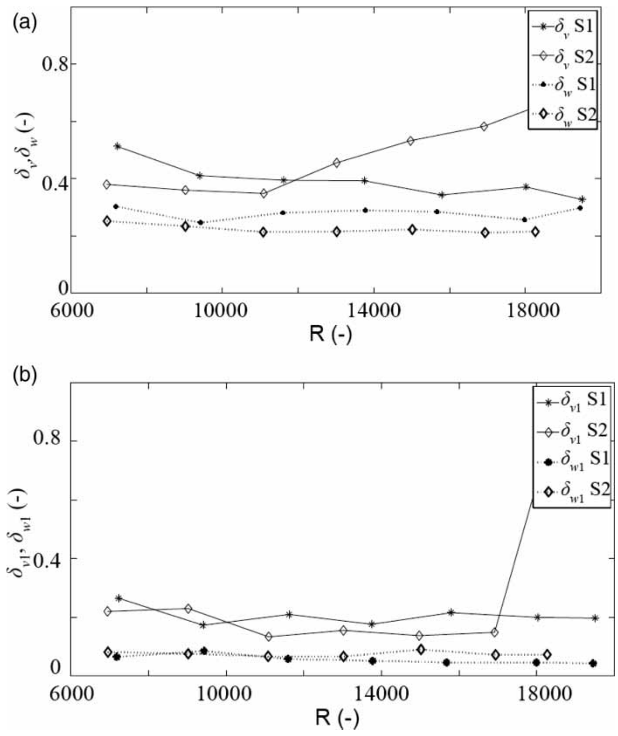

Figure 12 (a) Vortex thicknesses, (b) shear layer thicknesses versus R for various swirl vane configurations

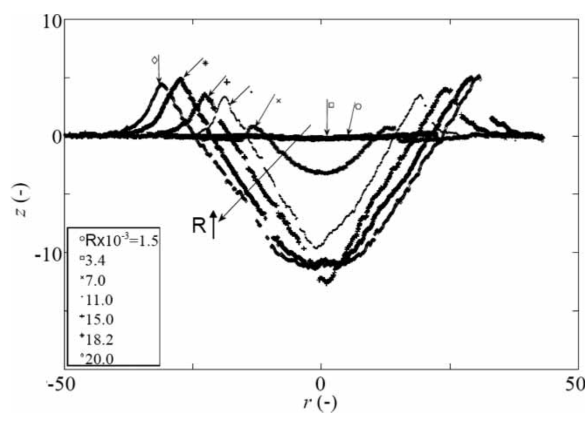

Figure 14 Non-dimensional contours of SAND1 bed scours for Case R, H/D = 30 and various R

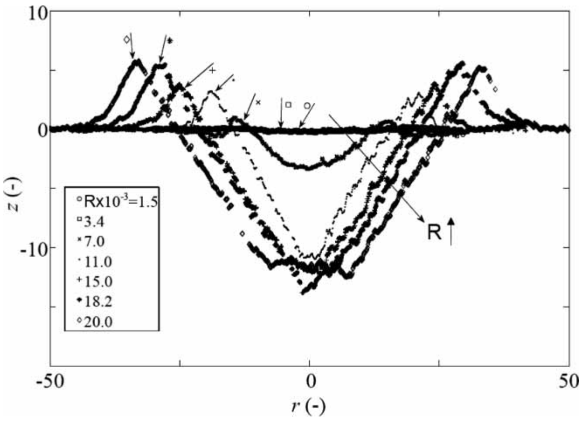

Figure 15 As Fig. 14, but for Case S1

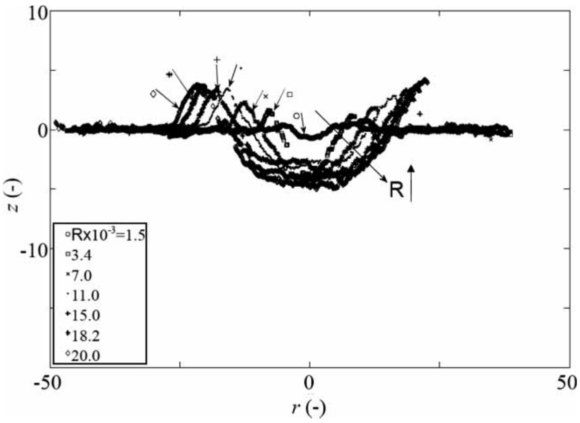

Figure 17 As Fig. 16, but for $H/D = 10$

distributions is defined as (Chigier and Chervinsky 1967)

$$q_i = \frac{\int_0^\infty r^2 W V \mathrm{d}r}{(D/2)\int_0^\infty r\big(W^2 - (1/2)V^2\big)\mathrm{d}r}. \qquad (7)$$

This swirl number is appropriate for any tangential velocity distribution. As shown in Fig. 13, the qualitative behaviour of this integral swirl number with R is surprisingly similar to q, even for Case S2, only their numerical values are smaller. Thus, one may use q, q_i, or even q_v, which is also proportional to q, to characterize the relative swirl intensity of various swirling jets.

3.2 *Scour patterns on sand beds*

Figures 14–17 show non-dimensional contours of the scour patterns on SAND1 bed generated by Cases S1 and S2 for various distances H/D as R is varied. Figures 14–16 relate to the largest nozzle-to-bed distance $H/D = 30$ for Cases R, S1 and S2, respectively. Note that the scour patterns for Case R and Case S1 are similar, whereas the scour patterns generated by Case S2 are much deeper and wider. As the distance to the bed decreases (Figs 16 and 17), both the depth and the crater radius on the sand bed generated by Case S2 decrease substantially, without a significant difference between $H/D = 10$ and $H/D = 5$ (not shown because it is similar to $H/D = 10$).

All this is better seen from Figs 18–20, showing the evolution of $H_{\min}$, $H_{\max}$ and $r_{\max}$ with R for Cases R, S1 and S2 impinging on the SAND1 bed for three distances H/D. Note that the best excavation performance results from Case S2, that imparts the maximum swirl to the jet, for $H/D = 30$. In this case, the scour hole is wider and deeper than for Cases R and S1, and Case S2 for $H/D = 5$ or $H/D = 10$, and the scour size depends less on R than for the other distances to the bed. Also, once a nozzle is selected, the scour patterns are almost identical for $H/D = 5$ and $H/D = 10$. The crater for $H/D = 30$ is also deeper for all R. For the two smallest distances, $H/D = 5$ and 10, the scour size $r_{\max}$ grows linearly with R, almost independently of the swirl vane configuration. For $H/D = 5$, the radial nozzle (R) generates deeper and wider scour holes for all R, i.e. for small distances, an axial jet produces a deeper and wider scour. For $H/D = 10$ and low R, Case S2 gives a deeper and wider scour, while for high R, Case R makes a deeper and wider scour, so that for medium distances, the final scour size depends on the nozzle.

Case S2 therefore represents the optimum for seabed excavation, especially for the largest distances considered and for

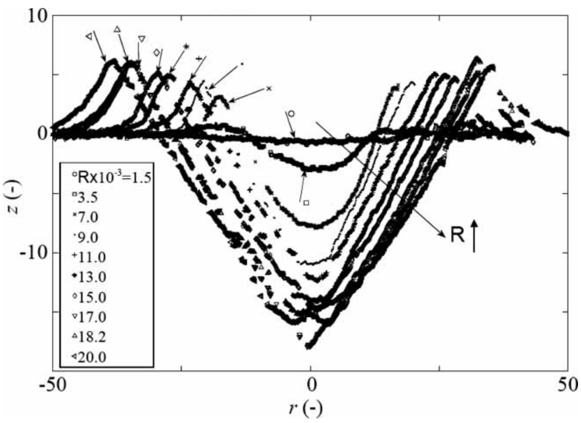

Figure 16 Non-dimensional contours of SAND1 bed scour for Case S2, $H/D = 30$ and various R

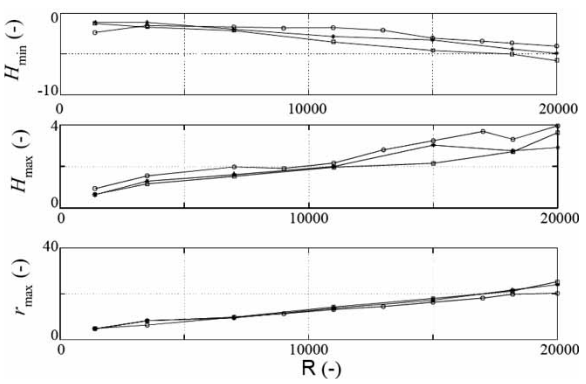

Figure 18 $H_{\min}$, $H_{\max}$ and $r_{\max}$ versus R for Cases (□) R, (*) S1 and (o) S2, $H/D = 5$. SAND1

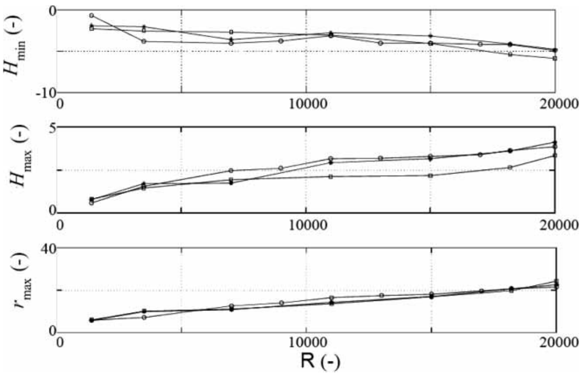

Figure 19 As Fig. 18, but for $H/D = 10$

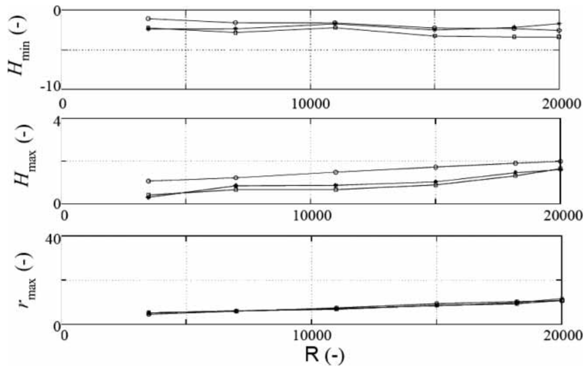

Figure 21 $H_{\min}$, $H_{\max}$ and $r_{\max}$ versus R for Cases (□) R, (*) S1 and (o) S2, SAND2 with $H/D = 5$

the highest Reynolds numbers. This can be explained by the special features of the swirling jet generated by the S2 nozzle above a certain threshold Reynolds number (Fig. 9): the axial velocity has a marked "overshoot" at the axis that increases the eroding jet power; additionally, for R $>$ 12,000, the swirling jet develops towards an annular region of high swirl, and almost swirl-free core inside, favouring the radial sediment dispersion uplifted by the more intense axial jet.

All experiments reported above for SAND1 were repeated using SAND2. The main results are summarized in Figs 21 and 22, where the evolution of the scour size parameters with R and H/D are stated for Cases R, S1 and S2. Note that the smallest value of R used with SAND1 bed has not been considered with SAND2. With the coarser sand, the excavation efficiency of all nozzles is poorer, with $|H_{\min}|$ and $r_{\max}$ almost half of the values obtained with SAND1. Yet the overall behaviour in terms of H/D and the swirl intensity are almost identical, except for $H/D = 30$ and Case S2 (Figs 20 and 22): the high excavation efficiency of SAND1 obtained with Case S2 for large H/D is not attained if the swirling jet impinges on coarse sand. A swirling jet is thus more efficient for sand bed excavation, especially for large R, if the nozzle-to-bed distance is sufficiently large, and the mean grain diameter $d_{50} < 1$ mm. The swirl effect is "lost" for sand beds with roughly $d_{50} > 1$ mm.

To our knowledge, no previous quantitative results on the scour patterns generated by a swirling jet impinging against a sand bed exist. Aderibigbe and Rajaratnam (1996) reported the maximum scour depth produced by a submerged, non-swirling jet for impinging distances ranging from $H/D = 5$ to $H/D = 125$. Their sand grains used were different to the mean sand sizes of SAND1 and SAND2 used herein, but the jet Reynolds number of one of their experiments is close to R $=$ 11,000 as used herein. Figure 23 compares the corresponding results for the scour depth $|H_{min}|$ versus H/D with the present results for SAND1 (note that their mean grain diameter was 0.88 mm). Our measured value of $|H_{\min}|$ for Case R and $H/D = 30$ is comparable to theirs, while the scour depth generated by the swirling jet S2 is larger, and the scour depth for Case S1 is in between. Note that R $=$ 11,000 is just below the threshold Reynolds number above which our Case S2 has the best excavation performance for $H/D = 30$. Marked in the figure is also the present maximum scour depth for $H/D = 30$ and S2, which is substantially larger.

Another interesting feature observed by Aderibigbe and Rajaratnam (1996) is that the scour depth increases with the impinging distance up to a maximum (at $H/D \cong 65$ for the case in Fig. 23), and then reduces. Such high values of H/D were not reached with our current experimental facility, but a similar trend is expected since the best results apply for $H/D = 30$.

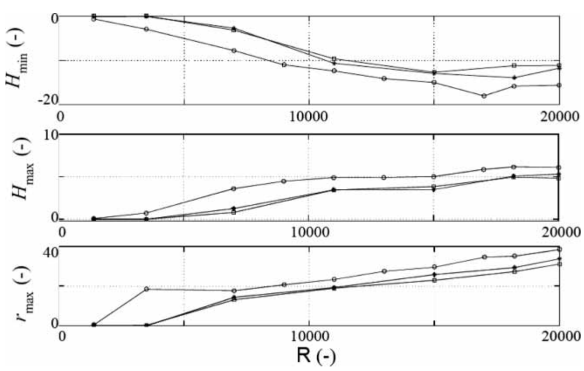

Figure 20 As Fig. 18, but for $H/D = 30$

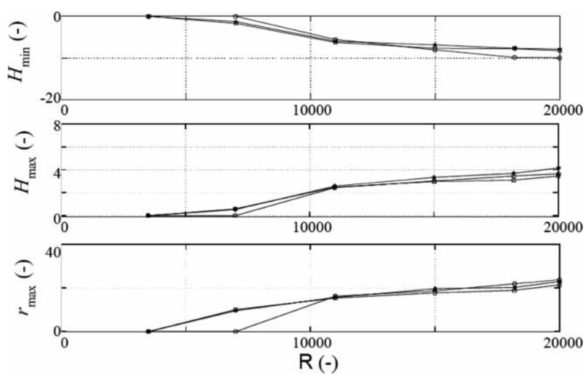

Figure 22 As Fig. 21, but for $H/D = 30$

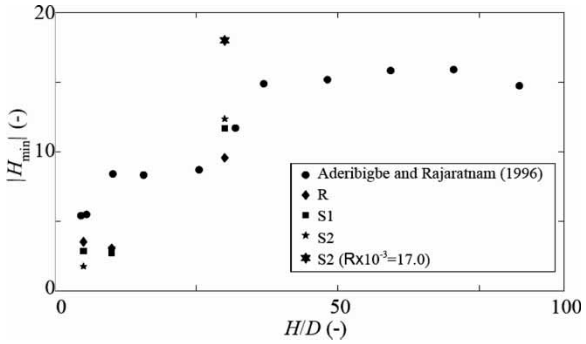

Figure 23 Comparison of results of Aderibigbe and Rajaratnam (1996) for $|H_{\min}|$ versus H/D with present results for SAND1 bed, R $=$ 11,000 and three nozzle configurations. Also include is result for R $=$ 17,000 and Case S2

4 Conclusions

The excavation performance of several swirling jets impinging normally against a sediment bed has been investigated experimentally for various distances from the nozzle to the bed, nozzle Reynolds numbers ranging between 1400 and 20,000, and two different sand grain diameters. Quantitative measurements of the scour patterns show that submerged swirling jets generated by nozzles with adjustable vanes are more efficient for sediment bed excavation than non-swirling jets if the nozzle Reynolds number is high enough for the jet to adopt an annular swirl structure combined with an intense axial velocity overshoot at the axis, which is achieved in this study only with the most tangential vane set (Case S2). A threshold Reynolds number of about 12,000 for Case S2 marks the transition to this jet flow structure, as characterized by LDA measurements at the nozzle exit. This jet structure generates a scour pattern whose diameter and depth are about twice of the scour hole generated by a non-swirling jet for the same Reynolds number, provided that the nozzle-to-bed distance is at least dozens of nozzle exit diameters and the grains have mean diameter of less than 1 mm. The range of Reynolds numbers considered is too narrow to study this jet transition in a nozzle with less swirl generation (Case S1).

Acknowledgement

This research was supported by the Ministerio de Educación y Ciencia of Spain, grant No. FIS2007-60161.

Notation

a, b = non-dimensional fitting parameters (–)
d_{50} = mean grain diameter (mm)
D = nozzle exit diameter (mm)
H = distance between sand and nozzle (mm)
$H_{\max}$ = non-dimensional maximum scour height (–)
$H_{\min}$ = non-dimensional scour depth (–)
q_i = integral swirl number (–)
q_v = swirl number (–)
q = swirl number used in q-vortex (–)
Q = discharge (m^3/s)
r = non-dimensional radial coordinate (–)
$r_{\max}$ = non-dimensional scour hole radius (–)
r_v, r_w = non-dimensional fitting parameters (–)
R = Reynolds number (–)
T = Temperature (K)
V = non-dimensional tangential velocity (–)
W = non-dimensional axial velocity (–)
W_c = mean axial velocity (m/s)
z = non-dimensional axial coordinate (–)
δ_v, δ_w = velocity core thicknesses (–)
δ_{v1}, δ_{w1} = velocity shear layer thicknesses (–)
ρ = fluid density (kg/m^3)
σ = sediment non-uniformity coefficient (–)
μ = fluid viscosity (kg/m s)
μ_0 = reference viscosity (kg/m s)

References

Aderibigbe, O.O., Rajaratnam, N. (1996). Erosion of loose beds by submerged circular impinging vertical turbulent jets. *J. Hydraulic Res*. 34(1), 19–33.

Andreotti, B., Claudin, P., Pouliquen, O. (2006). Aeolian sand ripples: experimental study of fully developed states. *Phys. Rev. Letts*. 96(2), 028001(4).

Ash, R.L., Khorrami, M.R. (1995). Vortex stability. *Fluid vortices*, 8, 317-372, S.I. Green, ed. Kluwer, Dordrecht NL.

Batchelor, G.K. (1964). Axial flow in trailing line vortices. *J. Fluid Mech*. 20, 645–658.

Bombardelli, F.A., Gioia, G. (2006). Scouring of granular beds by jet-driven axisymmetric turbulent cauldrons. *Phys. Fluids* 18(8), 088101.

Chigier, N.A., Chervinsky, A. (1967). Experimental investigation of swirling vortex motion in jets. *J. Appl. Mech*. 34(6), 443–451.

Dantec (2000). BSA/FVA Flow Software. http://www.dantecdynamics.com/.

Felli, M., Falchi, M., Pereira, J.A. (2010). Distance effect on the behavior of an impinging swirling jet by PIV and flow visualizations. *Exp. Fluids*. 48(2), 197–209.

Garg, A.K., Leibovich, S. (1979). Spectral characterization of vortex breakdown flowfields. *Phys. Fluids* 22(11), 2053–2064.

Gioia, G., Bombardelli, F.A. (2005). Localized turbulent flows on scouring granular beds. *Phys. Rev. Lett*. 95(14), 014501.

Hamill, G.A., Johnston, H.T., Stewart, P.D. (1999). Propeller wash scour near quay walls. *J. Wtrwy., Port, Coast, Oc. Eng*. 125(4), 170–175.

Hogg, A.J., Huppert, H.E., Dade, W.B. (1997). Erosion by planar turbulent wall jets. *J. Fluid Mech*. 338, 317–340.

Kobus, H., Leister, P., Westrich, B. (1979). Flow field and scouring effects of steady and pulsating jets impinging on a movable bed. *J. Hydraulic Res*. 17(3), 175–192.

Leibovich, S. (1978). The structure of vortex breakdown. *Ann. Rev. Fluid Mech*. 10, 221–346.

Lucca-Negro, O., O'Doherty, T. (2001). Vortex breakdown: a review. *Prog. Energy Combust. Sci*. 27(4), 431–481.

Michalke, A. (1984). Survey on jet instability theory. *Prog. Aerospace Sci*. 21(3), 159–199.

Ortega-Casanova, J., Martin-Rivas, S., del Pino, C. (2007). Research to evaluate the technological application of swirling jets in the field of sea-bed excavation, vessel propulsion and underwater cleaning. *Tech. Rept*. CRAFT project no. COOP-CT-2005-017725. D-9. Universidad de Málaga, Málaga.

Perng, A.T.H., Capart, H. (2008). Underwater sand bed erosion and internal jump formation by travelling plane jets. *J. Fluid Mech*. 595, 1–43.

Qi, M.L., Fujisak, M.L., Tanaka, K. (2000). Sediment re-suspension by turbulent jet in an intake pond. *J. Hydraulic Res*. 38(5), 323–330.

Rajaratnam, N. (1981). Erosion by plane turbulent jets. *J. Hydraulic Res*. 19(4), 339–358.

Rajaratnam, N., Berry, B. (1977). Erosion by circular turbulent wall jets. *J. Hydraulic Res*. 15(3), 277–289.

Redding, J. (2006). Dredging, scouring, excavation and cleaning. *US Patent Application*, US 2006/0151631 A1.

Rouse, H. (1940). Criteria for similarity in the transportation of sediment. Proc. Hydraulic Conf., Studies in Engineering. *Bulletin*. 20, 32–49, Univ. of Iowa, Iowa City.

'Swirl Jet Project'. (2007). http://www.swirljet.net

Thomas, R., Peakall, J., Simmons, S. (2007). Research to evaluate the technological application of swirling jets in the field of sea-bed excavation, vessel propulsion and underwater cleaning. *Tech. Report*, CRAFT project no. COOP-CT-2005-017725, D-14. University of Leeds, Leeds UK.

White, F.M. (2005). *Fluid mechanics* (5th ed.). McGraw-Hill, New York.

Young, I.T., Gerbrands, J.J., van Vliet, L.J. (1996). *Image processing fundamentals*. TU Delft, Delft (http://www.ph.tn.tudelft.nl/Courses/FIP/noframes/fip.html).